

A Continuous-Time Zoom ADC for Low-Power Audio Applications

Gonen, Burak; Karmakar, Shoubhik; van Veldhoven, Robert; Makinwa, Kofi A.A.

DOI

[10.1109/JSSC.2019.2959480](https://doi.org/10.1109/JSSC.2019.2959480)

Publication date

2020

Document Version

Final published version

Published in

IEEE Journal of Solid-State Circuits

Citation (APA)

Gonen, B., Karmakar, S., van Veldhoven, R., & Makinwa, K. A. A. (2020). A Continuous-Time Zoom ADC for Low-Power Audio Applications. *IEEE Journal of Solid-State Circuits*, 55(4), 1023-1031. Article 8945179. <https://doi.org/10.1109/JSSC.2019.2959480>

Important note

To cite this publication, please use the final published version (if applicable). Please check the document version above.

Copyright

Other than for strictly personal use, it is not permitted to download, forward or distribute the text or part of it, without the consent of the author(s) and/or copyright holder(s), unless the work is under an open content license such as Creative Commons.

Takedown policy

Please contact us and provide details if you believe this document breaches copyrights. We will remove access to the work immediately and investigate your claim.

Green Open Access added to TU Delft Institutional Repository

'You share, we take care!' - Taverne project

<https://www.openaccess.nl/en/you-share-we-take-care>

Otherwise as indicated in the copyright section: the publisher is the copyright holder of this work and the author uses the Dutch legislation to make this work public.

A Continuous-Time Zoom ADC for Low-Power Audio Applications

Burak Gönen¹, Shoubhik Karmakar², *Student Member, IEEE*, Robert van Veldhoven³, *Senior Member, IEEE*, and Kofi A. A. Makinwa⁴, *Fellow, IEEE*

Abstract—This article presents a continuous-time zoom analog to digital converter (ADC) for audio applications. It employs a high-speed asynchronous SAR ADC that dynamically updates the references of a continuous-time delta-sigma modulator (CTDSM). Compared to previous switched-capacitor (SC) zoom ADCs, its input impedance is essentially resistive, which relaxes the power dissipation of its reference and input buffers. Fabricated in a 160-nm CMOS process, the ADC occupies 0.27 mm² and achieves 108.1-dB peak SNR, 106.4-dB peak signal to noise and distortion ratio (SNDR), and 108.5-dB dynamic range in a 20-kHz bandwidth while consuming 618 μ W. This results in a Schreier figure of merit (FoM) of 183.6 dB.

Index Terms—A/D conversion, asynchronous SAR analog to digital converter (ADC), audio ADC, continuous-time delta-sigma, delta-sigma ADC, dynamic zoom ADC, inverter-based operational transconductance amplifier (OTA), low-power circuits.

I. INTRODUCTION

AUDIO analog to digital converters (ADCs) used in battery-powered devices are required to have high linearity and high dynamic range (DR) while also being energy efficient. These requirements can be met by the so-called zoom ADCs that are the hybrid combinations of SAR and delta-sigma ADCs [1], [2]. However, previous designs employed switched-capacitor (SC) front ends that required input and reference drivers capable of delivering large signal-dependent peak currents. For high linearity applications (>90 dB), the power dissipation of these drivers will be higher than that of the ADC itself, in some cases necessitating on-chip buffers, at the expense of chip area [3]. Previous zoom ADCs also required a first-order input filter to prevent aliasing and also to prevent them from overloading in the presence of large out-of-band signals [1], [2].

It is well known that ADCs based on the continuous-time delta-sigma modulators (CTDSMs) generally do not require anti-aliasing filters, while their resistive input impedance is easy to drive [3]. However, their design can be quite challenging. First, the linearity of the amplifiers used to realize their

first integrators is quite critical [4]. Apart from directly introducing harmonic distortion, amplifier non-linearity degrades the SNR by folding out-of-band quantization noise into the signal band. However, achieving high linearity usually increases power consumption. To mitigate this, circuit-level techniques to assist the first integrator have been proposed [5], [6]. Although effective, these methods increase design complexity. Another way of mitigating the effect of amplifier nonlinearity is to reduce the first integrator's input swing. This can be done by using a multi-bit digital to analog converter (DAC) or by using a DAC that incorporates a finite impulse response (FIR-DAC) filter [7]. Furthermore, CT DACs suffer from intersymbol interference (ISI), which manifests itself as distortion. Calibration [7], [8], dual return-to-zero (RTZ) switching [9], or digital ISI shaping techniques [10] have been proposed to mitigate ISI-induced distortion. These techniques considerably increase system complexity and degrade energy efficiency. Also, $1/f$ noise is a dominant noise source in audio CTDSMs. Chopping could be used to suppress $1/f$ noise, but this requires care due to chopping-related artifacts in CTDSMs [7], [11].

We propose a CT zoom ADC that achieves 108.1-dB peak SNR, 106.4-dB peak signal to noise and distortion ratio (SNDR), and 108.5-dB DR in a 20-kHz bandwidth while dissipating only 618 μ W [12]. This performance is achieved by combining an asynchronous 5-bit SAR ADC with a third-order single-bit CTDSM. For improved energy efficiency and linearity, its first integrator is based on a capacitively coupled inverter-based operational transconductance amplifier (OTA) that is chopped to mitigate its $1/f$ noise. The DAC employs a novel ISI reduction technique based on a matched-pair layout.

This article is organized as follows. Section II provides a brief introduction to the CT zoom ADC architecture and describes the system design of the ADC along with the error sources and the system-level techniques used to mitigate them. Section III discusses the circuit implementation. The experimental results are presented in Section IV. Finally, this article ends with conclusions.

II. CONTINUOUS-TIME ZOOM ADC

The block diagram of the proposed CT zoom ADC is shown in Fig. 1. It consists of an N -bit coarse SAR ADC and a 1-bit fine CTDSM that operate concurrently. The digital output of the coarse ADC, k , satisfies $k \cdot V_{\text{LSB},C} < V_{\text{in}} < (k + 1) \cdot V_{\text{LSB},C}$, where V_{in} is the input signal and $V_{\text{LSB},C}$ is the coarse quantization step or least significant bit (LSB). Via the multi-bit DAC shown in Fig. 1,

Manuscript received August 19, 2019; revised October 23, 2019; accepted November 24, 2019. Date of publication December 30, 2019; date of current version March 26, 2020. This article was approved by Guest Editor Brian Ginsburg. (Corresponding author: Burak Gönen.)

B. Gönen was with the Department of Microelectronics, Delft University of Technology, 2628 CD Delft, The Netherlands, and also with Broadcom, 3981 AJ Bunnik, The Netherlands. He is now with Ethernova, 3702 AA Zeist, The Netherlands (e-mail: b.gonen@tudelft.nl).

S. Karmakar and K. A. A. Makinwa are with the Department of Microelectronics, Delft University of Technology, 2628 CD Delft, The Netherlands.

R. van Veldhoven is with NXP Semiconductors, 5656 AE Eindhoven, The Netherlands.

Color versions of one or more of the figures in this article are available online at <http://ieeexplore.ieee.org>.

Digital Object Identifier 10.1109/JSSC.2019.2959480

0018-9200 © 2019 IEEE. Personal use is permitted, but republication/redistribution requires IEEE permission. See <https://www.ieee.org/publications/rights/index.html> for more information.

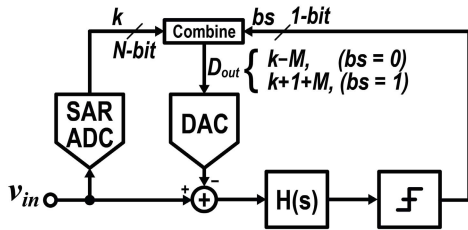
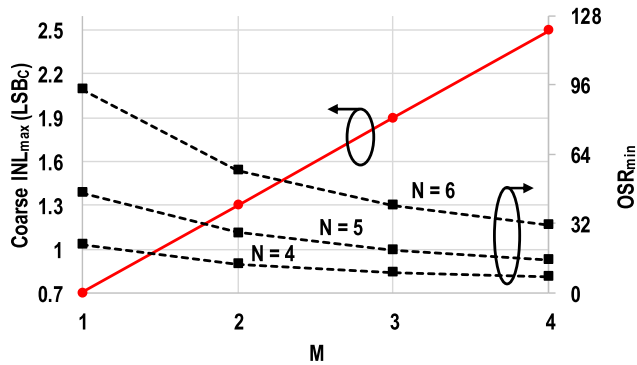


Fig. 1. Block diagram of the CT zoom ADC.

Fig. 2. Acceptable coarse ADC INL level and minimum OSR versus over-ranging factor (M).

the digital value k is used to dynamically adjust the references of the CTDSM such that

$$V_{\text{REF,DSM}} = (k + 1 + M) \cdot V_{\text{LSB,C}} \quad (1)$$

$$V_{\text{REF,DSM}} = (k - M) \cdot V_{\text{LSB,C}} \quad (2)$$

where M is an over-ranging factor. Driven by the modulator's bitstream (bs), the DAC then toggles between these references, effectively zooming in on V_{in} .

The use of over-ranging ensures that the input signal always lies in the modulator's stable input range even if the coarse ADC is not perfectly linear or if there is a mismatch between the coarse and fine quantization levels. For different values of M , the simulated integral nonlinearity (INL) of the coarse ADC that results in less than 10-dB signal to quantization noise ratio (SQNR) degradation is shown in Fig. 2. It can be seen that as M increases, the linearity requirement on the coarse ADC becomes increasingly relaxed.

If the slope of V_{in} becomes too large, the coarse ADC will not be able to update the fine ADC's references fast enough, leading to increased distortion [1], [2]. This is due to the delay between the sampling moment of the coarse ADC and the moment that its output is used by the DAC. In [2], this delay was minimized by using an asynchronous SAR ADC and by ensuring that its output was transferred to the DAC within half a sampling clock period.

In this article, the same approach is used. By using the analysis in [2] and assuming a full-scale input signal, the maximum input frequency ($F_{\text{in,max}}$) that the zoom ADC can handle can then be expressed as

$$F_{\text{in,max}} = \frac{\alpha(M + 0.5)2F_{\text{BW}}\text{OSR}}{\pi(2^N - 1)} \quad (3)$$

where α is a coefficient that defines the maximum stable input range, F_{BW} is the signal bandwidth, and OSR is the over-sampling ratio ($= F_S/2F_{\text{BW}}$). The minimum OSR, OSR_{min} , required to ensure that $F_{\text{in,max}} \geq F_{\text{BW}}$ for different values of

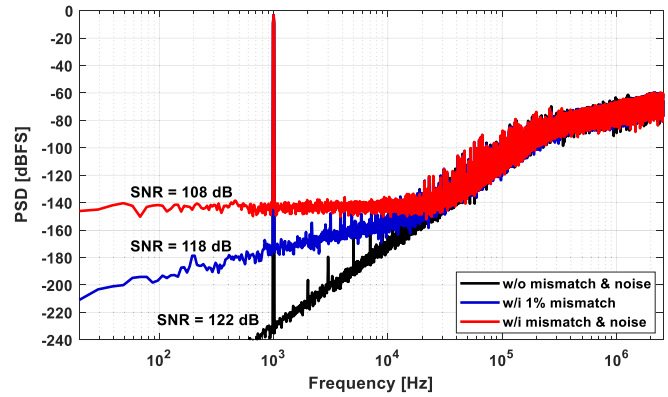


Fig. 3. Output spectra of the CT zoom ADC with different error sources.

M and N is shown in Fig. 2. It can be seen that for a given M , increasing N also increases OSR_{min} .

A previous SC zoom ADC intended for audio applications achieved 103-dB SNDR with the help of a third-order loop filter, $N = 5$, $M = 2$, and $\text{OSR} = 282$ [1]. However, its coarse ADC required five clock cycles per conversion, so the use of a faster ADC should enable a significant reduction in OSR. This would reduce the power dissipated by the clock generator, the quantizer, and the digital logic, which is quite significant in the chosen 160-nm process. From Fig. 2, OSR_{min} is found to be roughly 40 for $N = 5$ and $M = 1$, while simulations show that an OSR of ~ 64 is commensurate with a target SNDR of 108 dB (the same as in [1]).

The use of data weighted averaging (DWA) to linearize the zoom ADC's multi-bit DAC puts a higher limit on OSR because it only provides 1st-order mismatch shaping while the CTDSM has a higher-order noise shaping. It also puts a lower limit on OSR due to the level of unit mismatch, below which the shaped mismatch error is too high for the targeted SNDR. Thus, in order to find the optimum OSR, first, an acceptable unit mismatch should be chosen depending on the technology and area restrictions. Assuming a third-order loop filter, $M = 1$, $N = 5$, and 1% unit mismatch, $\text{OSR} = 128$ is found to be the optimum where the contributions of shaped quantization noise and shaped mismatch error are equal at the signal band edge. This is shown in the output spectra obtained from the behavioral simulations shown in Fig. 3 for three different scenarios: no mismatch and thermal noise, 1% unit mismatch and no thermal noise, and both 1% mismatch and thermal noise. The resulting in-band SNR is 122, 118, and 108 dB, respectively. From Fig. 2, these parameters also ensure that the criterion $F_{\text{in,max}} \geq F_{\text{BW}}$ is satisfied with adequate margin.

III. CIRCUIT IMPLEMENTATION

A simplified schematic of the implemented CT zoom ADC is shown in Fig. 4. It consists of a 5-bit asynchronous SAR ADC, a third-order feed-forward compensated loop filter, a 1-bit quantizer, and a 5-bit unary resistive DAC (R-DAC).

A. Loop Filter

As shown in Fig. 4, the CIFF loop filter used in the proposed CT zoom ADC is implemented with active-RC integrators.

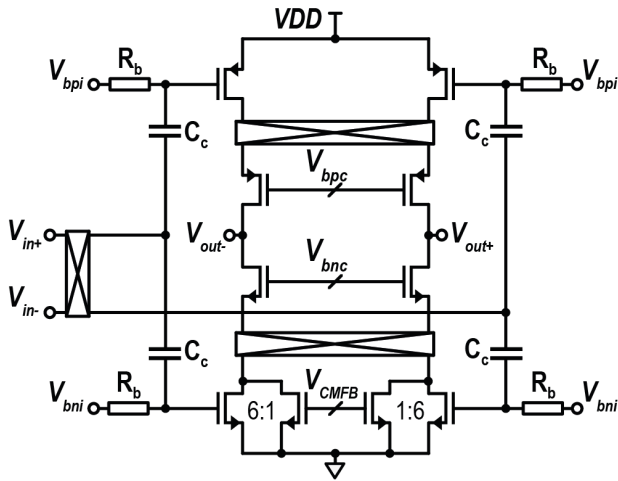


Fig. 6. Simplified schematic of the proposed amplifier.

into an output dc current. In this way, the high-pass filter's corner frequency only has to be lower than F_{chop} . To avoid down-converting the quantization noise present at the virtual ground node, the choppers are driven at the sampling frequency ($F_{\text{chop}} = F_S$) [7], [11]. Since the output choppers are placed in a high bandwidth node between the input devices and the cascodes, the dc gain reduction due to these is negligible.

For linearity, the coupling capacitors ($C_c = 2$ pF) are implemented as metal fringe capacitors and designed to be much larger than the gate capacitances of the input transistors to minimize signal attenuation. The polysilicon biasing resistors ($R_b = 3$ M Ω) are chosen to ensure that the high-pass corner frequency is much less than F_S . In the layout, R_b is placed under C_c to reduce the total area of the four R_b - C_c pairs to 0.01 mm².

The NMOS input transistors are split in a 6:1 ratio, with the smaller branch being used for common-mode feedback (CMFB). A CT CMFB circuit is used to sense and stabilize the amplifier's output common-mode voltage [17]. The input and output choppers also chop the offset and low-frequency noise contributed by the CMFB loop itself.

Simulations were made to compare the linearity of the proposed amplifier with that of its fully differential counterpart. Both the amplifiers are biased in weak inversion, have the same I_{bias} and device sizing, and thus have the same power consumption and g_m . In Fig. 7, the nonlinear components of their differential output currents are shown after being normalized to I_{bias} . It can be seen that the proposed capacitively coupled pseudo-differential amplifier is much more linear than its fully differential counterpart. In fact, it requires $2\times$ less power for the same linearity. A detailed analysis of the linearity of both amplifiers is given in the Appendix.

The total power consumption of the amplifier is 205 μ W, including the chopper drivers, biasing, and CMFB circuits. Its nominal and minimum dc gains are 60 and 55 dB, respectively, over process, voltage and temperature (PVT) (-55 $^{\circ}$ C– 150 $^{\circ}$ C and 1.6–2 V), as shown in Fig. 8. The amplifier's simulated CMRR is greater than 70 dB up to 1 kHz. Its simulated PSRR is greater than 100 dB up to 1 kHz and greater than 50 dB for higher frequencies due to chopping.

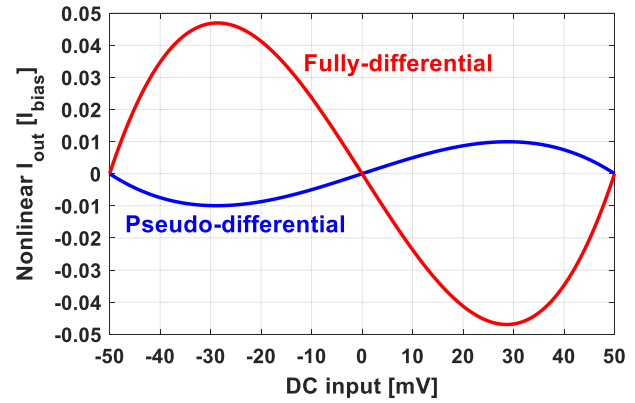


Fig. 7. Nonlinear components of I_{out} for a fully differential and pseudo-differential amplifiers.

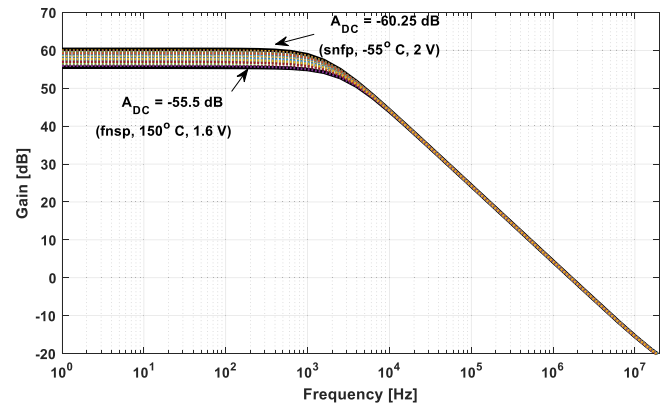


Fig. 8. OTA gain over PVT.

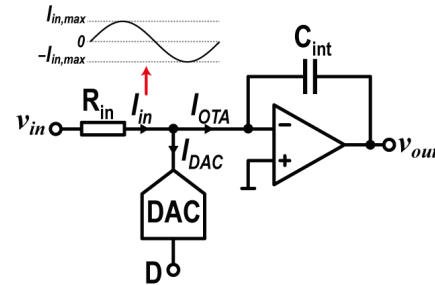


Fig. 9. I_{DAC} and I_{OTA} for NRZ and RZ DACs.

C. DAC

The DAC of the zoom ADC is one of its most critical blocks, as it directly impacts its total input-referred noise, total harmonic distortion (THD), and clock jitter sensitivity. An NRZ DAC is preferred for high energy efficiency and low jitter sensitivity. The input voltage is converted to a current (I_{in}) via R_{in} , as shown in Fig. 9. After subtracting the DAC current (I_{DAC}), their difference (I_{OTA}) is then integrated. The maximum value of I_{OTA} defines the output current requirements of the OTA and hence its power consumption. The maximum input current ($I_{\text{in,max}}$) for a sinusoidal input with amplitude $V_{\text{in,max}}$ is

$$I_{\text{in,max}} = \frac{V_{\text{in,max}}}{R_{\text{in}}}. \quad (4)$$

Fig. 10 shows I_{OTA} and I_{DAC} for NRZ and RZ DACs for a zoom ADC based on a 3-bit coarse ADC. For an NRZ DAC,

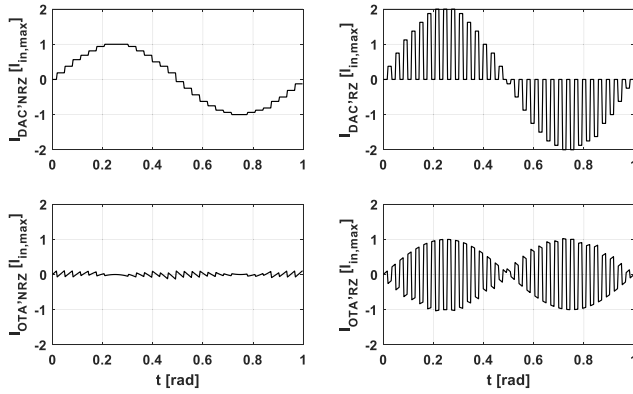
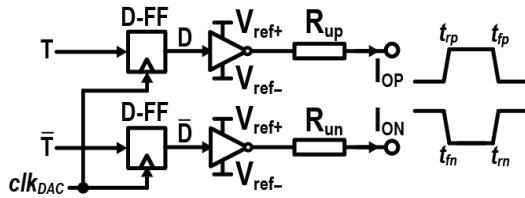
Fig. 10. I_{DAC} and I_{OTA} for NRZ and RZ DACs.

Fig. 11. Schematic of an R-DAC cell.

the difference between I_{in} and I_{DAC} is constant and decreases as the resolution of the coarse DAC is increased. For an RZ DAC, however, this difference is much larger, since I_{DAC} is sometimes zero, and so I_{OTA} should be as large as $I_{\text{in,max}}$. Moreover, the jitter sensitivity of an NRZ DAC is considerably better than that of an RZ DAC.

There are two ways to implement a two-level NRZ DAC: as a current DAC (I-DAC) or as an R-DAC. However, an IDAC will generate extra distortion due to the interaction between the nonlinear output impedance of its current sources and the voltage swing at the virtual ground of the OTA. An R-DAC is not only more linear, but it also has lower thermal and $1/f$ noise [18]. Thus, an R-DAC is used in this article.

ISI refers to the signal-dependent errors that occur at code transitions due to the finite rise/fall times of the currents generated by the unit elements of the R-DAC. The use of DWA makes this problem even worse because it increases the number of unit element transitions in the DAC and introduces even-order distortion [10]. In this article, a novel ISI reduction technique is proposed to solve this problem.

In the output of the differential R-DAC unit element shown in Fig. 11, there are four different transition edges: t_{rp} , t_{rn} , t_{fp} , and t_{fn} . If the total amount of positive and negative DAC output currents within one period would match, there would be no nonlinear ISI error [10]. One approach to achieve this is to match a rising edge with its corresponding falling edge (match t_{rp} and t_{fn} , and match t_{rn} and t_{fp}) [7], [8]. However, this is hard to guarantee in practice since the speed of the rising edges is set by PMOS drivers, while the speed of the falling edges is set by NMOS drivers. Thus, background calibration is often necessary for this approach [7], [8].

Alternatively, we note that to avoid ISI, it is only necessary to match the rising and falling edges of the positive and the negative half DACs (match t_{rp} and t_{rn} , and match t_{fp} and t_{fn}). This is comparatively easy to achieve because the edges that

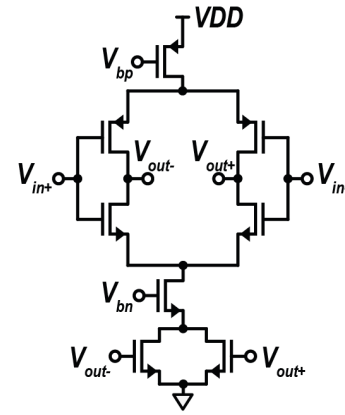


Fig. 12. Amplifiers used in the second and third integrators.

need to be matched are generated by the same type of devices. However, the positive and the negative DAC unit resistors also need to match, as they also influence the resulting rise and fall times. Simulations indicated that the 1% matching needed for low DWA in-band noise (IBN) is also more than enough to achieve < -120 -dB HD_2 . The positive and negative half DACs should then be laid out next to each other. Noting that the ON resistances of the DAC switches are much smaller than R_{up} and R_{un} , the matching requirements on the driver inverters can be relaxed to 5%. The switch driving signal asymmetry, which is also a source of ISI error, is reduced by using two separate flip-flops to drive D and \bar{D} , as shown in Fig. 11.

D. Amplifiers of the Second and Third Integrators

The noise and distortion specifications of the second and third integrators are relaxed by the gain preceding them. They are implemented with current-starved inverters as shown in Fig. 12, each consuming $15 \mu\text{W}$ while providing 45-dB dc gain.

E. Asynchronous SAR ADC and Alias Rejection

The asynchronous SAR ADC used in this article is similar to the one in [2], but with smaller DAC unit capacitors (1.8 fF) to reduce the peak currents drawn from the input, resulting in a total sampling capacitance of 55 fF.

Due to its input sampler, the asynchronous SAR ADC could alias the signals around F_S back to dc. This could be prevented by utilizing an all-pass filter [19]. However, the passive elements required to implement an all-pass filter for the chosen F_S would occupy a large area. In this article, we propose to use a simple first-order RC low-pass filter as shown in Fig. 4 to suppress the signal components around F_S instead. Simulations showed that $R_{\text{filt}} = 20 \text{ k}\Omega$ and $C_{\text{filt}} = 5 \text{ pF}$ are enough to achieve better than 65-dB alias rejection around F_S .

IV. MEASUREMENT RESULTS

As shown in Fig. 13, the prototype CT zoom ADC occupies 0.27 mm^2 in a 160-nm CMOS technology. The input resistors, R-DAC, loop filter, SAR ADC, and digital logic occupy 18%, 18%, 53%, 4%, and 7% of the total area, respectively.

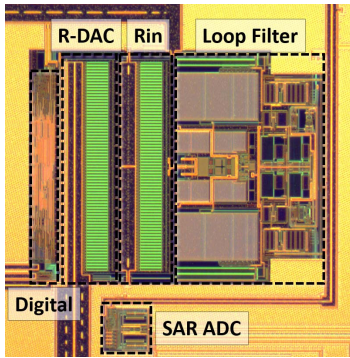


Fig. 13. Chip micrograph.

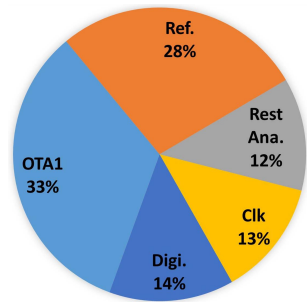
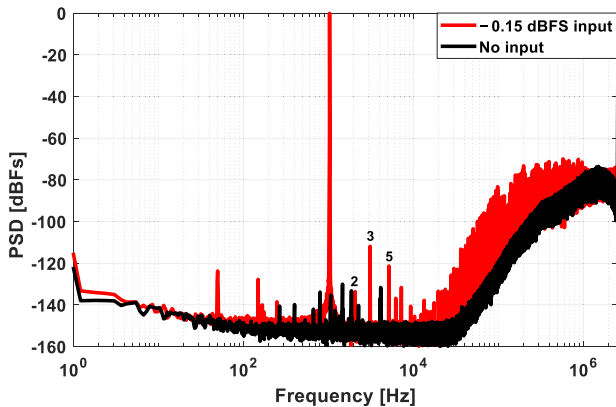


Fig. 14. Power breakdown.

Fig. 15. Measured output spectrum (-0.15 -dBFS input signal at 1 kHz, and no signal. 2^{23} points 8 average with Hanning window).

The ADC consumes $618 \mu\text{W}$ from a 1.8 -V supply. The analog, reference, clock, and digital circuitry consume 45% , 28% , 13% , and 14% , respectively, of this total power. As shown in Fig. 14, the first integrator dominates the analog power consumption. The voltage references are externally generated ($V_{\text{ref}+} = 1.8$ V and $V_{\text{ref}-} = 0$ V).

The measured output spectrum of the ADC is shown in Fig. 15. When no input signal applied ($V_{\text{in}} = 0$), the ADC effectively operates like a third-order 1-bit DSM. The in-band tones seen in this case are due to DWA. Peak SNDR is achieved with an input of -0.15 dBFS. HD_3 is the dominant distortion component at -113 dB, and all other harmonic components are below -120 dB. The tones at 50 and 150 Hz are due to the signal generator. The measured peak SNR,

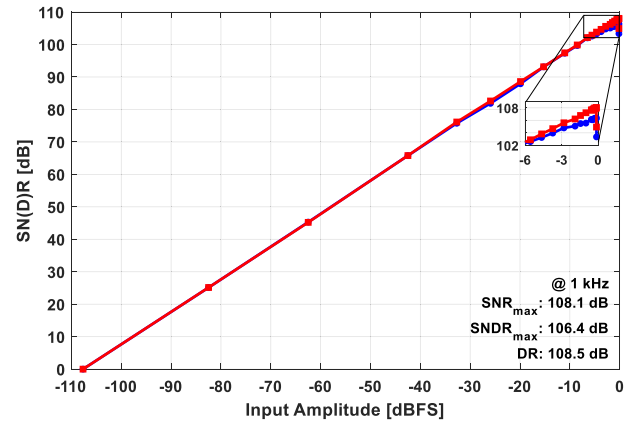
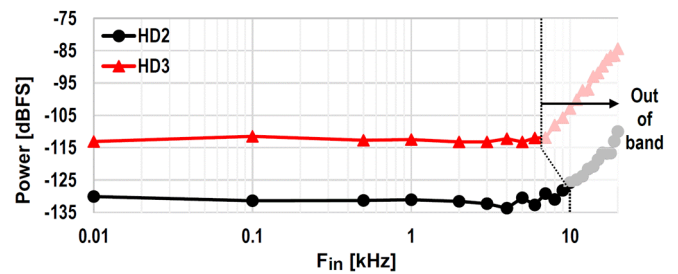
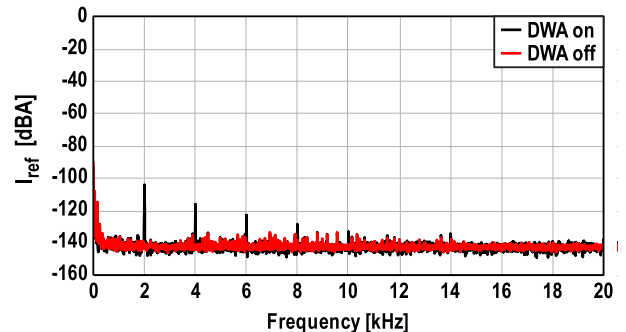


Fig. 16. Measured SNR and SNDR across input amplitude.

Fig. 17. HD_2 and HD_3 versus F_{in} .Fig. 18. Measured I_{ref} power spectrum for DWA ON and OFF.

SNDR, and DR are 108.1 , 106.5 , and 108.5 dB, respectively (see Fig. 16).

Fig. 17 shows the HD_2 and HD_3 levels for -1 -dBFS single-tone in-band input signals. HD_3 is lower than -113 dB and HD_2 is lower than -125 dB for all frequencies. Low HD_2 levels prove the efficacy of the proposed ISI mitigation technique. The apparent increase in HD_2 and HD_3 at higher frequencies is due to the increased quantization noise at these frequencies. The measured INL of the SAR ADC is 0.15 LSB $_C$.

The signal-dependent unit transitions caused by DWA make the current drawn from the reference signal-dependent [10]. To illustrate this, the current drawn from $V_{\text{ref}+}$, I_{ref} , is measured with an audio analyzer. The measured power spectrum of I_{ref} is shown in Fig. 18 for $F_{\text{in}} = 1$ kHz and for DWA "ON" and "OFF." It can be seen that DWA causes even-order tones

TABLE I
PERFORMANCE SUMMARY AND COMPARISON WITH PREVIOUS WORK

	This work	JSSC'18 Jang [6]	JSSC'18 Karmakar [2]	JSSC'17 Gönen [1]	JSSC'17 Billa [7]	JSSC'16 Berti [21]	JSSC'16 Leow [22]	TCAS-I'16 Lee [16]
Architecture	CT Zoom	CT 1.5-Bit	SC Zoom	SC Zoom	CT FIRDAC	CT Multi-Bit	CT Multi-Bit	SC Single-Bit
Tech (nm)	160	65	160	160	180	160	65	180
Area (mm²)	0.27	0.14	0.25	0.16	1	0.21	0.25	0.31
Supply (V)	1.8	1.2	1.8	1.8	1.8	1.6	1	1.8
Power (μW)	618	68	280	1120	280	390	800	300
F_s (MHz)	5.12	6.144	2	11.3	6.144	3	6.4	6.1
Bandwidth (kHz)	20	24	1	20	24	20	25	20
SNR (dB)	108.1	94.8	119.1	106	99.3	93.4	100.1	98.6
SNDR (dB)	106.4	94.1	118.1	103	98.5	91.3	95.2	97.7
DR (dB)	108.5	98.2	120.3	109	103.6	103.1	103	100.5
FoM_{S,SNDR}⁺ (dB)	181.5	179.5	183.6	175.5	177.8	170.5	170.1	175.9
FoM_{S,DR}⁺⁺ (dB)	183.6	183.6	185.8	181.5	182.9	180.2	177.9	178.7

⁺FoM_{S,SNDR} = SNDR + 10log(BW/Power) ⁺⁺FoM_{S,DR} = DR + 10log(BW/Power)

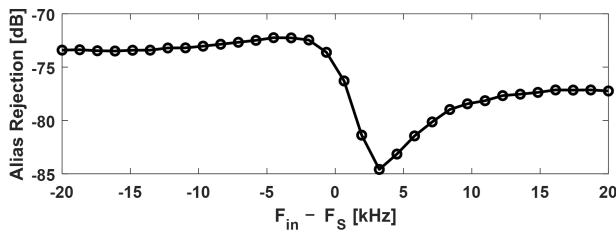


Fig. 19. Measured alias rejection properties of the CT zoom ADC.

in I_{ref} . The mixing of these even-order components with the input signal via the finite output impedance of the reference is thus the main reason for the odd-order harmonic components (HD₃₋₉) seen in Fig. 15.

The ADC's measured CMRR and PSRR at 50 Hz are greater than 70 and 100 dB, respectively, and its $1/f$ corner is lower than 20 Hz, demonstrating the performance benefits of the capacitively coupled chopped OTA. The measured alias rejection of the ADC is then higher than -72 dB for -6 -dBFS input signals, as shown in Fig. 19.

Table I summarizes the performance of the proposed CT zoom ADC and compares it with that of other state-of-the-art audio ADCs. The proposed ADC outperforms all the others in terms of peak SNDR and Schreier figure of merit (FoM). Although the SC zoom ADC presented in [1] achieves a similar peak DR and SNR, it requires much stronger input drivers. The input impedance of the proposed CT zoom ADC is essentially resistive and so can be easily driven.

V. CONCLUSION

A CT zoom ADC to digitize audio signals with the state-of-the-art energy efficiency has been presented. The combination of a fast 5-bit asynchronous SAR ADC and a 5-bit NRZ DAC significantly reduced the input swing applied to a fine 1-bit CTDSM, thus significantly reducing its required linearity

and power consumption. By implementing the first stage of the DSM with a highly linear capacitively coupled pseudo-differential amplifier, the ADC's energy efficiency is further improved. To reduce the potential ISI caused by its resistor DAC, a simple ISI-reducing layout technique is proposed and proven. Taken together, these techniques result in the state-of-the-art energy efficiency.

APPENDIX

LINEARITY ANALYSIS OF FULLY DIFFERENTIAL PSEUDO-DIFFERENTIAL INPUT PAIRS

In this appendix, an analysis of the input pairs shown in Fig. 5 is performed to compare their linearity. In order to not limit the analysis to only one operation region, i.e., weak, moderate, or strong inversion, the transconductance-to-current ratio (g_m/I_d)-based method in conjunction with the Enz, Krummenacher, Vittoz (EKV) model proposed in [20] is used. The drain current of a transistor in saturation

$$I_D = 2nV_T^2\mu C_{ox}\frac{W}{L}(q^2 + q) \quad (5)$$

where q is the normalized mobile charge density at the source, n is the subthreshold slope, and V_T is the thermal voltage. The relationship between the gate drive voltage and q is given as

$$V_{GS} - V_{TH} = nV_T[2(q - 1) + \log(q)] \quad (6)$$

where V_{TH} is the threshold voltage. g_m/I_D could be then found as [20]

$$\frac{g_m}{I_D} = \frac{1}{nV_T} \frac{1}{q + 1}. \quad (7)$$

Due to the differential operation, even-order nonlinearity components will be zero. For this analysis, we will take only the third-order distortion into account. The output current then be written by using the power series expansion

$$i_d = g_{m1}v_{gs} + \frac{1}{6}g_{m3}v_{gs}^3 \quad (8)$$

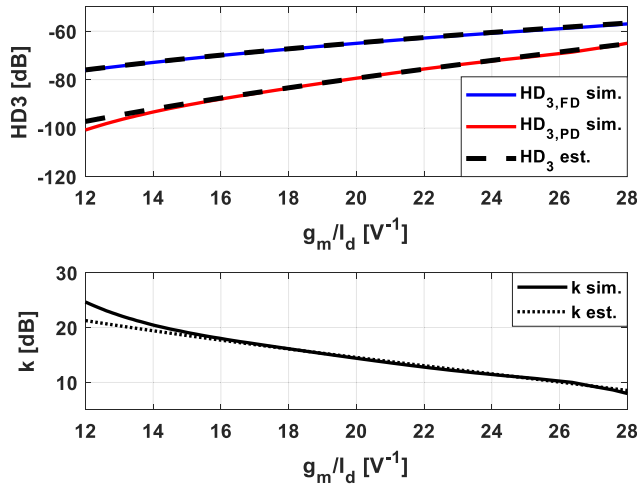


Fig. 20. HD₃ and k versus g_m/I_D for pseudo-differential and fully differential input pairs ($L = 0.7 \mu\text{m}$).

g_{m1} and g_{m3} are given in [20] for a common-source stage as

$$g_{m1} = I_s \left(\frac{1}{nV_T} \right) q$$

$$g_{m3} = I_s \left(\frac{1}{nV_T} \right)^3 \frac{q}{(2q+1)^3}. \quad (9)$$

HD₃ could be found for the pseudo-differential input pair shown in Fig. 19 by using (4)–(8) for a differential sinusoidal input signal with $v_{i,\text{pk}}$ amplitude

$$\text{HD}_{3,\text{PD}} \approx \frac{1}{16} \left| \frac{g_{m3}}{6g_{m1}} \right| v_{i,\text{pk}}^2 = \frac{1}{96} \left(\frac{1}{nV_T} \right)^2 \frac{1}{(1+2q)^3} v_{i,\text{pk}}^2. \quad (10)$$

The HD₃ of the fully differential input pair is found in [20]

$$\text{HD}_{3,\text{FD}} = \frac{1}{24} \left(\frac{1}{nV_T} \right)^2 \frac{(1+3q)}{2(1+2q)^3} v_{i,\text{pk}}^2. \quad (11)$$

The ratio of HD_{3,FD} to HD_{3,PD} is then found as

$$k = \frac{\text{HD}_{3,\text{FD}}}{\text{HD}_{3,\text{PD}}} = 2 + 6q. \quad (12)$$

Using (4)–(6), we can find k in terms of g_m/I_D , n , and V_T

$$k = \frac{6}{\frac{g_m}{I_D} n V_T} - 4. \quad (13)$$

The only one process parameter required for this equation is n . g_m/I_D is a very useful design parameter that determines the achievable g_m for a given bias current I_D .

Fig. 20 shows the simulated HD₃ and k for the fully differential and pseudo-differential NMOS input pairs for different g_m/I_D values, both driven by a sinusoidal input with $v_{i,\text{pk}} = 10 \text{ mV}$. The HD₃ and k values estimated by (10) and (11) after extracting $n = 1.25$ from the used 160-nm process are also shown in dashed lines. The simulated and estimated results are in good agreement, and they show that for all operation regions, the pseudo-differential pair is more linear than its fully differential counterpart. k is at least 8 dB for weak inversion (high g_m/I_D), and it increases to more than 20 dB for strong inversion (lower g_m/I_D). Note that the earlier

analysis and simulations do not include the output impedance nonlinearity.

REFERENCES

- [1] B. Gönen, F. Sebastiano, R. Quan, R. van Veldhoven, and K. A. A. Makinwa, "A dynamic zoom ADC with 109-dB DR for audio applications," *IEEE J. Solid-State Circuits*, vol. 52, no. 6, pp. 1542–1550, Jun. 2017.
- [2] S. Karmakar, B. Gönen, F. Sebastiano, R. van Veldhoven, and K. A. A. Makinwa, "A 280 μW dynamic zoom ADC with 120 dB DR and 118 dB SNDR in 1 kHz BW," *IEEE J. Solid-State Circuits*, vol. 53, no. 12, pp. 3497–3507, Dec. 2018.
- [3] K. Nguyen, R. Adams, K. Sweetland, and H. Chen, "A 106-dB SNR hybrid oversampling analog-to-digital converter for digital audio," *IEEE J. Solid-State Circuits*, vol. 40, no. 12, pp. 2408–2415, Dec. 2005.
- [4] P. Sankar and S. Pavan, "Analysis of integrator nonlinearity in a class of continuous-time delta-sigma modulators," *IEEE Trans. Circuits Syst. II, Exp. Briefs*, vol. 54, no. 12, pp. 1125–1129, Dec. 2007.
- [5] S. Pavan and P. Sankar, "Power reduction in continuous-time delta-sigma modulators using the assisted opamp technique," *IEEE J. Solid-State Circuits*, vol. 45, no. 7, pp. 1365–1379, Jul. 2010.
- [6] M. Jang, C. Lee, and Y. Chae, "Analysis and design of low-power continuous-time delta-sigma modulator using negative-R assisted integrator," *IEEE J. Solid-State Circuits*, vol. 54, no. 1, pp. 277–287, Jan. 2018.
- [7] S. Billa, A. Sukumaran, and S. Pavan, "Analysis and design of continuous-time delta-sigma converters incorporating chopping," *IEEE J. Solid-State Circuits*, vol. 52, no. 9, pp. 2350–2361, Sep. 2017.
- [8] T. He, M. Ashburn, S. Ho, Y. Zhang, and G. Temes, "A 50 MHz-BW continuous-time $\Delta\Sigma$ ADC with dynamic error correction achieving 79.8 dB SNDR and 95.2 dB SFDR," in *IEEE ISSCC Dig. Tech. Papers*, Feb. 2018, pp. 230–232.
- [9] R. Adams and K. Q. Nguyen, "A 113-dB SNR oversampling DAC with segmented noise-shaped scrambling," *IEEE J. Solid-State Circuits*, vol. 33, no. 12, pp. 1871–1878, Dec. 1998.
- [10] L. Risbo, R. Hezar, B. Kelleci, H. Kiper, and M. Fares, "Digital approaches to ISI-mitigation in high-resolution oversampled multi-level D/A converters," *IEEE J. Solid-State Circuits*, vol. 46, no. 12, pp. 2892–2903, Dec. 2011.
- [11] H. Jiang, B. Gönen, K. A. A. Makinwa, and S. Nihitanov, "Chopping in continuous-time sigma-delta modulators," in *Proc. IEEE Int. Symp. Circuits Syst. (ISCAS)*, May 2017, pp. 1–4.
- [12] B. Gönen, S. Karmakar, R. van Veldhoven, and K. A. A. Makinwa, "A low power continuous-time zoom ADC for audio applications," in *Proc. Symp. VLSI Circuits*, Jun. 2019, pp. 224–225.
- [13] S. Pavan, R. Schreier, and G. C. Temes, *Understanding Delta-Sigma Data Converters*, Hoboken, NJ, USA: Wiley, 2017.
- [14] M. Bolatkale, L. J. Breems, R. Rutten, and K. A. A. Makinwa, "A 4 GHz continuous-time $\Delta\Sigma$ ADC with 70 dB DR and -74 dBFS THD in 125 MHz BW," *IEEE J. Solid-State Circuits*, vol. 46, no. 12, pp. 2857–2868, Dec. 2011.
- [15] M. S. Akter, R. Sehgal, F. Goes, K. A. A. Makinwa, and K. Bult, "A 66-dB SNDR pipelined split-ADC in 40-nm CMOS using a class-AB residue amplifier," *IEEE J. Solid-State Circuits*, vol. 53, no. 10, pp. 2939–2950, Oct. 2018.
- [16] S. Lee, W. Jo, S. Song, and Y. Chae, "A 300- μW audio $\Delta\Sigma$ modulator with 100.5-dB DR using dynamic bias inverter," *IEEE Trans. Circuits Syst. I Reg. Papers*, vol. 63, no. 11, pp. 1866–1875, Nov. 2016.
- [17] J. H. Huijsing, R. Hogervorst, and K. J. D. Langen, "Low-power low-voltage VLSI operational amplifier cells," *IEEE Trans. Circuits Syst. I, Fundam. Theory Appl.*, vol. 42, no. 11, pp. 841–852, Nov. 1995.
- [18] P. Shettigar and S. Pavan, "Design techniques for wideband single-bit continuous-time $\Delta\Sigma$ modulators with FIR feedback DACs," *IEEE J. Solid-State Circuits*, vol. 47, no. 12, pp. 2865–2879, Dec. 2012.
- [19] P. Cenci *et al.*, "A 3.2 mW SAR-assisted CT $\Delta\Sigma$ ADC with 77.5 dB SNDR and 40 MHz BW in 28 nm CMOS," in *IEEE Symp. VLSI Circuits Dig.*, Jun. 2019, pp. 230–231.
- [20] P. G. A. Jespers and B. Murmann, "Calculation of MOSFET distortion using the transconductance-to-current ratio (g_m/I_D)," in *Proc. IEEE Int. Symp. Circuits Syst. (ISCAS)*, vol. 2015, pp. 529–532.
- [21] C. de Berti, P. Malcovati, L. Crespi, and A. Baschirotto, "A 106 dB A-weighted DR low-power continuous-time $\Delta\Sigma$ modulator for MEMS microphones," *IEEE J. Solid-State Circuits*, vol. 51, no. 7, pp. 1607–1618, Jul. 2016.

- [22] Y. H. Leow, H. Tang, Z. C. Sun, and L. Siek, "A 1 V 103 dB 3rd-order audio continuous-time $\Delta\Sigma$ ADC with enhanced noise shaping in 65 nm CMOS," *IEEE J. Solid-State Circuits*, vol. 51, no. 11, pp. 2625–2638, Nov. 2016.



Burak Gönen received the B.Sc. degree in electronics from Istanbul Technical University, Istanbul, Turkey, in 2012, and the M.Sc. degree (*cum laude*) in microelectronics from the Delft University of Technology, Delft, The Netherlands, in 2014, where he is currently pursuing the Ph.D. degree. His Ph.D. research is focusing on the design of energy- and area-efficient analog-to-digital converters for digital audio and sensor interfaces in collaboration with NXP Semiconductors, Eindhoven, The Netherlands.

From 2011 to 2012, he was an Intern with Mikroelektronik Ar-Ge Ltd., Istanbul. From 2013 to 2014, he was an Intern with NXP Semiconductors Research. From 2012 to 2019, he was with Electronic Instrumentation Laboratory, Delft University of Technology. In 2019, he was a Senior Analog IC Design Engineer with Broadcom, Bunnik, The Netherlands. Recently, he joined Ethernova, Zeist, The Netherlands, as a Senior Member of Technical Staff. His current research interests include high-performance data converters for wireline communications.

Mr. Gönen was awarded with the First Prize at the IEEE SSCS Benelux Chapter Student Chip Design Contest in 2017.



Shoubhik Karmakar (S'18) received the B.E. degree in electrical and electronics engineering from the Birla Institute of Technology and Science, Chiclim, India, in 2012, and the M.Sc. degree from the Delft University of Technology, Delft, The Netherlands, in 2017, where he is currently pursuing the Ph.D. degree in collaboration with NXP Semiconductors, Eindhoven, The Netherlands, with a focus on high-power Class-D amplifiers.



Robert van Veldhoven (SM'12) was born in Eindhoven, The Netherlands, in 1972. He received the Ph.D. degree in electrical engineering from the University of Eindhoven, Eindhoven, The Netherlands.

In 1996, he joined Philips Research, Eindhoven, and moved to NXP Semiconductors, Eindhoven, in 2006, where he is currently an Architect leading a team of 15 engineers working on automotive grade data converters and sensor interfaces. He holds over 25 US patents and (co-)authored more than 15 ISSCC/JSSC articles.

Mr. Veldhoven is also a reviewer for several professional journals and conferences. In 2004 and 2010, he was invited to give an ISSCC forum presentation on sigma-delta modulators for wireless and cellular receivers.



Kofi A. A. Makinwa (M'97–SM'05–F'11) received the B.Sc. and M.Sc. degrees from Obafemi Awolowo University, Ife, Nigeria, in 1985 and 1988, respectively, the M.E.E. degree from Philips International Institute, Eindhoven, The Netherlands, in 1989, and the Ph.D. degree from the Delft University of Technology, Delft, The Netherlands, in 2004.

From 1989 to 1999, he was a Research Scientist with Philips Research Laboratories, Eindhoven, where he worked on interactive displays and digital recording systems. In 1999, he joined the Delft

University of Technology, where he is currently an Antoni van Leeuwenhoek Professor and the Head of the Microelectronics Department. He has coauthored or edited 15 books and more than 250 technical articles. He holds 30 patents. His research interests include the design of mixed-signal circuits, sensor interfaces, and smart sensors.

Dr. Makinwa is also a member of the Royal Netherlands Academy of Arts and Sciences and the Editorial Board of the PROCEEDINGS OF THE IEEE. He was a recipient of the 2005 Simon Stevin Gezel Award from the Dutch Technology Foundation. He was a co-recipient of the 15 best paper awards from the IEEE JOURNAL OF SOLID-STATE CIRCUITS (JSSC), the International Solid-State Circuits Conference (ISSCC), the IEEE TRANSACTIONS ON VERY LARGE SCALE INTEGRATION (VLSI) SYSTEMS, the European Solid-State Circuits Conference (ESSCIRC), and *Transducers*. At the 60th anniversary of ISSCC, he was recognized as a Top-ten Contributor. He is also the Analog Subcommittee Chair of the ISSCC. He has served as a Distinguished Lecturer and an Elected AdCom Member for the IEEE Solid-State Circuits Society. He has been a Guest Editor of the IEEE JSSC. He serves on the Program Committees of the VLSI Symposium, ESSCIRC, and the Advances in Analog Circuit Design (AACD) Workshop.